# Mechanism of the High Tc superconducting dynamo, models and experiment.

Ratu Mataira,* Andres Pantoja, Rod Badcock, and Chris Bumby†
*Robinson Research Institute, Faculty of Engineering,*
*Victoria University of Wellington, 69 Gracefield Road, Lower Hutt 5010, New Zealand*

Mark Ainslie
*Department of Engineering, University of Cambridge,*
*Trumpington Street, Cambridge CB2 1PZ, United Kingdom*

High-$T_c$ superconducting (HTS) dynamos are experimentally proven devices that can produce large, >kA, DC currents in superconducting circuits, without the thermal leak associated with copper current leads. However, these DC currents are theoretically controversial, as it is not immediately apparent why a device that is topologically identical to an AC alternator should give a DC output at all. Here, we present a finite-element model, and its comparison with experiment, which fully explains this effect. It is shown that the DC output arises naturally from Maxwell's laws, when time-varying overcritical eddy currents are induced to circulate in an HTS sheet. We first show that our finite-element model replicates all of the the experimental electrical behavior reported so far for these devices, including the DC output characteristics, and transient electrical waveforms. Direct experimental evidence for the presence of circulating eddy currents is also obtained through measurements of the transient magnetic field profile across the HTS tape, using a linear Hall array. These results are also found to closely agree with predictions from the finite-element model. Following this experimental validation, calculated sheet current densities and the associated local electric fields are examined for a range of frequencies and net transport currents. We find that the electrical output from an HTS dynamo is governed by the competition between transport and eddy currents induced as the magnet transits across the HTS tape. These eddy currents are significantly higher (∼1.5X) than the local critical current density $J_c$, and hence experience a highly non-linear local resistivity. This non-linearity breaks the symmetry observed in a normal ohmic material, which usually requires the net transport current to vary linearly with the average electric field. The interplay between local current densities and non-linear resistivities (which both vary in time and space) is shown to systematically give rise to the key observed parameters for experimental HTS dynamo devices: the open-circuit voltage $V_{\rm oc}$, the internal resistance $R_{\rm int}$, and the short-circuit current $I_{\rm sc}$. Finally, we identify that the spatial boundaries formed by each edge of the HTS stator tape play a vital role in determining the total DC output. This offers the potential to develop new designs for HTS dynamo devices, for which the internal resistance is greatly reduced and the short circuit current is substantially increased.

## I. INTRODUCTION

High-$T_c$ Superconducting (HTS) dynamos [1–13], and other similar HTS 'flux pumps' [14–22] have received continued recent attention as they offer a potential solution to the DC current injection problem in a wide range of superconducting machines [23] and magnets [24, 25]. Specifically, the HTS dynamo is of interest for its predicted ability to drive large [26, 27] DC currents without the associated heat leak of traditional current leads [28]. This current is provided by a near-zero source impedance, which reduces the risk of an externally-initiated 'driven' quench[29, 30]. Such high-current low-impedance sources could enable new types of coil design which avoid many of the operating risks associated with high-inductance high-voltage superconducting coils [31, 32]. However, the DC output observed from experimental HTS dynamo devices [7] has presented physicists with a conundrum, as this device is topologically identical to an AC alternator as described by Faraday [33] and, hence should not be expected to produce a DC *emf*. This has led some authors to propose explanations based upon exotic phenomena such as quantum flux coupling [34] or flux ratcheting [21]. We have recently shown [12] that it is in fact, unnecessary to invoke such new physics as the DC output produced by an HTS dynamo arises naturally from Maxwell's laws, when applied to the situation in which eddy currents flow in a thin sheet exhibiting a highly non-linear local resistivity. Here, we now develop the model introduced in [12] to provide a detailed explanation of how the non-linear resistivity changes the electromagnetic physics of the HTS dynamo, and hence gives rise to the DC voltage component.

Simple application of Faraday's law to a closed path, $C$, experiencing a periodic applied magnetic field cycle, enables the time-averaged DC value of the *emf* to be stated as:

$$\int_t^{t+P} dt \oint_C d\vec{l}.\vec{E} = \Phi\big|_{t+P} - \Phi\big|_t = 0, \qquad (1)$$

where $\Phi$ is the magnetic flux enclosed by the path $C$,

* ratu.mataira@vuw.ac.nz
† chris.bumby@vuw.ac.nz

and $P$ is the period of the cycle. However, it should be noted that the *emf* and the output voltage are not necessarily identical, as the *emf* does not include any resistive potential drops which may occur between the device terminals. In the HTS dynamo, eddy-currents flow in the plane of the stator tape, and experience local flux-flow resistance which varies in both time and space over the duration of one cycle. To understand the impact of these locally circulating currents, we must therefore take care to formulate the underlying electromagnetic theory explicitly.

Finite element (FE) modeling now enables computation of the local current density at each point within an HTS conductor experiencing a time-varying applied magnetic field. Through using the $H$-formulation [35–39] of to solve Faraday's and Ampere's laws, an FE model of an HTS dynamo operating in the *open-circuit* condition has been produced [12]. This has been used to show that the open-circuit voltage output arises due to the presence large over-critical eddy currents which flow in the HTS stator for a short period of each rotor cycle, and act to 'partially rectify' the induced *emf*.

Here we now extend this FE model to the *closed-circuit* case, thus enabling current and voltage outputs to be fully calculated for the full range of operating conditions of the device. We show that this simple 2D model captures all of the essential electrical behavior which has been observed by experiment [3, 7, 40], including linear DC $I$-$V$ characteristics, linear frequency dependencies of both internal resistance and output voltages, and transient voltage waveforms. We also report further validation of the FE model through experimental measurements of the transient local magnetic field in the plane of the HTS stator tape, which confirm the presence of large over-critical circulating currents as the rotor magnet traverses the stator tape. Through interpreting results from the FE model, we find that both the short-circuit current ($I_{sc}$) and apparent internal resistance ($R_{int}$) of the dynamo, arise from competition between the net transport current $I_{\mathrm{T}}$ and the local circulating eddy currents. This understanding implies that HTS dynamo designs incorporating much wider stators should exhibit improved performance, as has been reported experimentally [9, 41].

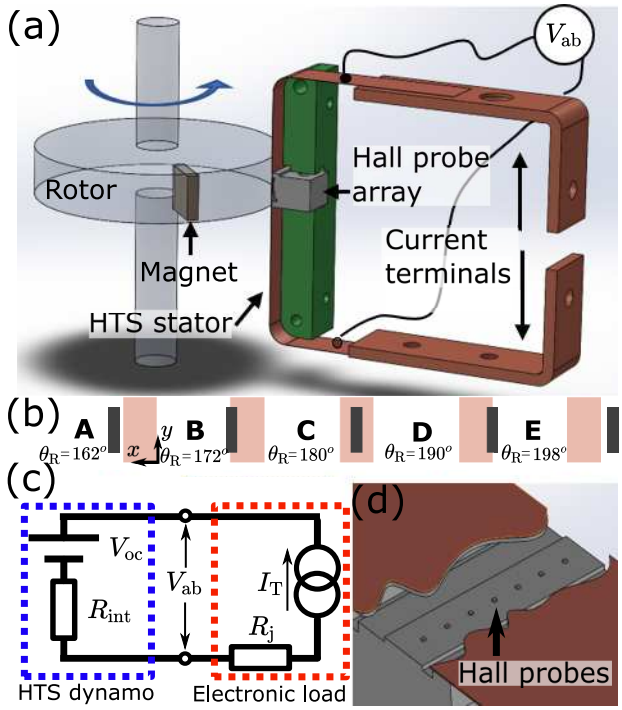


FIG. 1. (a) Schematic of the HTS dynamo, including the rotor magnet, rotor housing, HTS stator, voltage leads, Hall probe array, and the current terminations. (b) Illustrated key rotor positions $\theta_{\mathrm{R}}$, as viewed from the rotor. (c) Circuit diagram showing the dynamo as a voltage $V_{\mathrm{oc}}$ and internal resistance $R_{\mathrm{int}}$, and the current source, current leads, termination blocks, and joints combined into a single electronic load $R_{\mathrm{j}}$. (d) Cutaway from the rotor side of the stator showing the Hall probes in the array.

## II. EXPERIMENTAL METHODS

Data was collected using an experimental HTS dynamo similar to that studied in previous work [12, 40], and depicted in fig. 1(a). The dynamo stator is made from 12 mm wide SCS12050 AP SuperPower Inc HTS coated-conductor tape. The superconducting layer ( 1 $\mu$m thick) is deposited on a 50 $\mu$m thick Hastelloy substrate, which is then electroplated with 25 $\mu$m of copper stabilizer on each side of the tape. The transport critical current, $I_{\mathrm{c}}$, of the stator tape used here was measured and found to be 293 A at 77 K (using the 1 $\mu$V criterion). A 12.7 mm long, 12.7 mm deep and 3.2 mm wide Nd-Fe-B permanent magnet, magnetized through its depth, is mounted within an aluminum rotor such that the outer face of the magnet is rotated about a radius of 35 mm. The stator tape is positioned perpendicular the plane of rotation such that the vector normal to the tape surface faces in toward the rotor axis, with a flux gap $g$ of 3.7 mm between the stator tape and the rotor circumference. The ends of the stator tape are then soldered onto copper current leads that connect to an external electronic current supply. The combination of the leads and the external current supply act as an electronic load for the output of the HTS dynamo [5, 8], see fig. 1(c).

Voltage taps are positioned on the stator tape such that small variations in position do not alter the measured DC output from the device [7]. However, small displacements of the voltage tap leads will always change the inductive-*emf* pick up of the total loop. To remove the influence of the arbitrary *emf* pick up from the voltage tap leads, we make measurements of the device at both room temperature, $V_{300\mathrm{K}}$, and in liquid nitrogen, $V_{77\mathrm{K}}$, enabling differentiation between the signal obtained in the normal and superconducting states respectively. AQs long as the applied magnetic field is much higher than any internal field produced by induced eddy currents in the

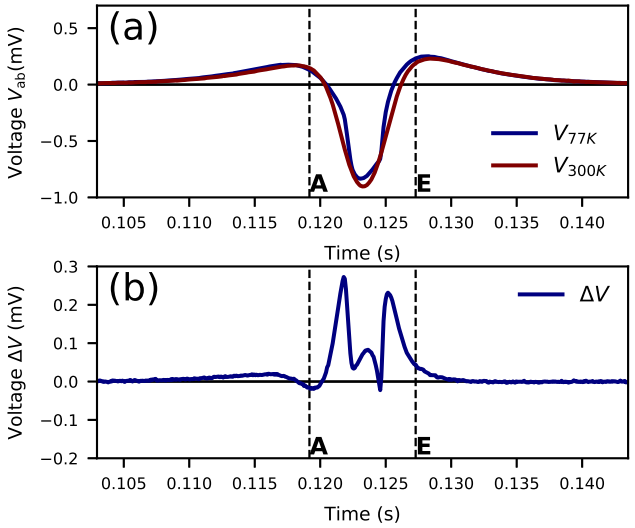


FIG. 2. (a) Comparison between 77K and 300K voltage pulse measurements for the dynamo operating at 12.33 Hz as the magnet transits the stator. (b) Voltage difference $\Delta V$, as defined in (2), showing a clear DC bias in the 77 K waveform.

HTS tape, $V_{300\mathrm{K}}$ can be considered a measurement of the *emf* induced by the magnet in the closed loop formed by the stator tape and tap leads. This allows us to define the difference between the induced *emf* and the actual measured voltage across the stator tape as:

$$\Delta V(t) = V_{77\mathrm{K}}(t) - V_{300\mathrm{K}}(t), \tag{2}$$

where we will reserve the symbol $\Delta$ for measurement differences between 77 K and 300 K. The *emf* -free quantity, $\Delta V(t)$, is independent of the placement of the voltage tap leads (as long as the voltage tap leads are mechanically fixed to prevent movement between the 77 K and 300 K measurements). An example open-circuit waveform for one rotor cycle is shown in fig. 2(b). An issue arises when seeking to measure the $\Delta V(t)$ waveforms in the presence of a net transport current $|I_{\mathrm{T}}| > 0$, as $V_{300\mathrm{K}}(t, I_{\mathrm{T}})$ is not available due to the inability to transport large currents through the stator in the normal conducting state at 300 K. Hence more generally, we define:

$$\Delta V(I_{\mathrm{T}}, t) = V_{77\mathrm{K}}(I_{\mathrm{T}}, t) - V_{300\mathrm{K}}(0, t). \tag{3}$$

where, $V_{300\mathrm{K}}(0, t)$ still captures the *emf* contribution assuming a static transport current.

While (2) allows us to examine the transient dynamics of the device during operation, the useful output of the device is its time-averaged DC voltage:

$$V_{\mathrm{dc}} = f \int_0^{1/f} V_{77\mathrm{K}} dt = f \int_0^{1/f} \Delta V dt, \tag{4}$$

where $f$ is the frequency of the rotor rotation. Note that at room temperature the integral of $V_{300\mathrm{K}}$ is zero as the device, when normal conducting, is equivalent to the classical AC alternator with a linear resistivity.

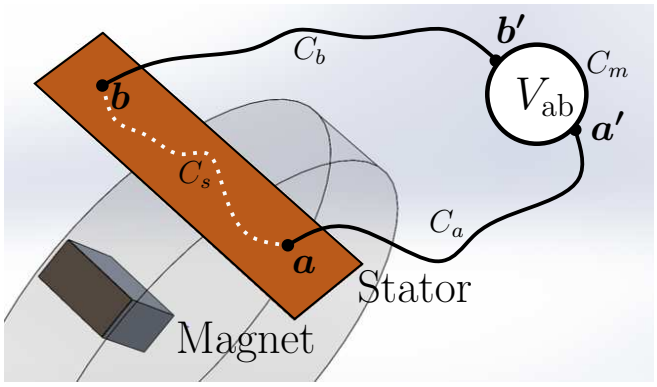


FIG. 3. The HTS stator and the attached voltage leads, forming the 4 sections of the Amperian loop $C$; through the sample $C_s$, through the two leads $C_a$, and $C_b$, as well as through the meter $C_m$.

Underneath the HTS stator tape, an array of 7 Arepoc cryogenic Hall probes are mounted approximately 0.5 mm away from the tape surface, measuring the component of the magnetic field perpendicular to the tape, $B_y$. Again, we make measurements of the magnetic field at 77 K, $B_{77\mathrm{K}}$, and 300 K, $B_{300\mathrm{K}}$. As the Nd-Fe-B magnet exhibits the same magnetization at these two temperatures, any difference between the measured magnetic fields must be caused by currents flowing in the HTS tape:

$$\Delta B(x, t) = B_{77\mathrm{K}}(x, t) - B_{300\mathrm{K}}(x, t) = \mu_0 H_y(x, t), \tag{5}$$

where $H_y$ is the perpendicular auxiliary field due to the free currents in the conductor.

The rotor and stator assembly of the device is placed in a bath cryostat, with 77 K measurements made following submerssion in liquid nitrogen. Mechanical power to the rotor is provided through a G10 composite shaft connected to an external stepper motor at room temperature. The stepper motor gives a selection of rotational frequencies, 178, 255, 365, 520, 740, 1051, and 1490 RPM. Measurements are taken using a single magnet in the rotor assembly, such that there is a 1:1 relation between motor speed and applied magnetic field frequency $f$ at the stator tape. At each rotor speed the full $I$-$V$ curve is examined by adjusting the net current flowing through the stator tape, using the Agilent 6680A #J04 current supply to step in 2 A increments.

## III. MODELLING, MEASUREMENT, AND THEORY

To investigate the physics underlying the measured voltages and magnetic fields, it is necessary to build a model of the given system. First we must clearly establish the relationship between the measured values and the physical fields which underlie them. We start with

the gauge invariant form of the electric field:

$$\vec{E} = -\vec{\nabla}\psi - \partial_t \vec{A}, \tag{6}$$

where $\vec{\nabla}\psi$ is the gradient of the scalar potential, and $\vec{A}$ is the magnetic vector potential. As explained well by Clem [42], any measured voltage $V_{\rm ab}$, such as $V_{300\rm K}$ or $V_{77\rm K}$, is given by the electric field in the meter itself. In the case of an ideal voltmeter, the active component is taken to be sufficiently small that $\partial_t \vec{A}$ is negligible, and the meter is only effected by the electrostatic potential $\vec{\nabla}\psi$ (see fig. 3. Therefore the value of $\vec{E}$ in the meter can be solved by solving for $\vec{\nabla}\psi$. As an integral of $\vec{\nabla}\psi$ between $\boldsymbol{a'}$ and $\boldsymbol{b'}$ is path independent, it must be equivalent to the integral along the nearly-closed loop made by the sample and the measurement leads, between the same points $\boldsymbol{a'}$ and $\boldsymbol{b'}$. Denoting the path through the leads as $C_l = C_a + C_b$, the path through the sample as $C_s$, and assuming $\vec{E} = 0$ in the leads, we can define a measured voltage $V_{\rm ab}$ as:

$$\begin{aligned} V_{\rm ab} &= \int_{C_m} \vec{\nabla}\psi \cdot d\vec{l} = \int_{C_s} \vec{\nabla}\psi \cdot d\vec{l} + \int_{C_l} \vec{\nabla}\psi \cdot d\vec{l} \\ &= -\int_{C_s} \vec{E} \cdot d\vec{l} - \int_{C_l + C_s} \partial_t \vec{A} \cdot d\vec{l} \\ &= -\int_{C_s} \vec{E} \cdot d\vec{l} - d_t \iint_{S_s} \vec{B} \cdot d\vec{s}, \end{aligned} \tag{7}$$

where we note that while the integral through $C_l + C_s$ is not closed, missing the contribution form $C_m$, as the length of $C_m$ tends to zero, this term captures the rate of change of the captured magnetic flux.

Re-examining the experimental logic behind (3), that $V_{300\rm K}$ is a measure of the *emf*, we can frame the approximation as a condition on the magnetic flux through the loop:

$$d_t \iint_{S_s} \vec{B}_{77K} \cdot d\vec{a} = d_t \iint_{S_s} \vec{B}_{300K} \cdot d\vec{a}. \tag{8}$$

We can not impose a more rigorous, local, or even weaker assumption on the fields at the different temperatures. Indeed, some local restriction of $B$ would invalidate (5).

With the approximation well defined, we may express $\Delta V$ from (7):

$$\Delta V = -\int_{C_s} \left(\vec{E}_{77K} - \vec{E}_{300K}\right) \cdot d\vec{l} \tag{9}$$

Focusing our analysis on the symmetric plane bisecting the dynamo, we can capture the necessary physics, without considering the nature of the integral paths. In the symmetric $x, y$ plane only currents into and out of the plane $J_z$ need to be considered. This of course limits $\vec{E}$ to $E_z$ as well. Furthermore, it can be shown that assuming reflectional symmetry along the plane forces $\vec{\nabla}\psi$ to be constant over the plane, up to a choice of gauge. Therefore, the spatial variations in $E_z$ can be attributed entirely to the changing vector potential $d_t A_z$. Hence, in the plane, $\vec{\nabla}\psi$ can be thought of as:

$$\begin{aligned} \vec{\nabla}\psi(x,y,z,t)|_{z=0} &= \partial_z \psi(t) \\ &= -E_z(x,y,t) - d_t A_z(x,y,t), \end{aligned} \tag{10}$$

which leads to the fact that only the spatially averaged components of both $E_z$ and $d_t A_z$ contribute to $\partial_z \psi$:

$$\begin{aligned} \partial_z \psi(t) &= \frac{1}{A}\int_\Omega \partial_z \psi(t) da \\ &= \frac{1}{A}\int_\Omega E_z(x,y,t) - d_t A_z(x,y,t) da \\ &= -E_{\rm ave} - d_t A_{\rm ave}. \end{aligned} \tag{11}$$

From (11) we can quickly examine Faraday's alternator, where for a homogeneous normal conductor, $E = \rho J$ implies $E_{\rm ave} = \rho J_{ave}$, i.e., Ohm's law. Then the AC alternator has a DC component proportional to the DC current flowing through the stator, and if that DC current is zero, then there is no DC output voltage. However, in the case of the superconductor $E = \rho(J)J$ does not imply $E_{\rm ave} = \rho(J_{ave})J_{ave}$.

Looking back at (2) and (9) and using the same assumptions, we can use (11) to define a similar state (super- vs normal-conducting) comparison for $\partial_z \psi$:

$$\begin{aligned} \Delta\partial_z \psi(I_{\rm T}, t) &= \partial_z \psi_{77K}(I_{\rm T}, t) - \partial_z \psi_{300K}(0, t) \\ &= -E_{\rm ave,77K}(I_{\rm T}, t), \end{aligned} \tag{12}$$

where again, the spatially averaged electric field at zero net current and room temperature $E_{\rm ave,300K} = 0$ V/m and the A vector is the same at both RT and 77 K $d_t A_{\rm ave,77K} = d_t A_{\rm ave,300K}$, which is true in the context of the full measurement loop, regardless of gauge as long as we assume (8).

If we make the simple approximation that the 3D system is translationally symmetric under the length of the magnet $L$, then the solution in plane can be extrapolated, and related to measurement:

$$\begin{aligned} \Delta V(I_{\rm T}, t) &= \int_{-L/2}^{L/2} \Delta\partial_z \psi(I_{\rm T}, t) dz \\ \Delta V(I_{\rm T}, t) &= -L \times E_{\rm ave,77K}(I_{\rm T}, t), \end{aligned} \tag{13}$$

where the *lhs* is measurable and the *rhs* can be calculated. For brevity, we will refer to $E_{\rm ave,77K}$ as simply $E_{\rm ave}$ from this point on.

## IV. MODEL CONSTRUCTION

In order to calculate $E_{\rm ave}(t)$ we must calculate the full solution for $E_z(x, y, t)$ in the modeled plane. To do this we use the $H$-formulation form of the finite element problem to solve Maxwell's equations. As argued, we take advantage of the device's reflectional symmetry to reduce

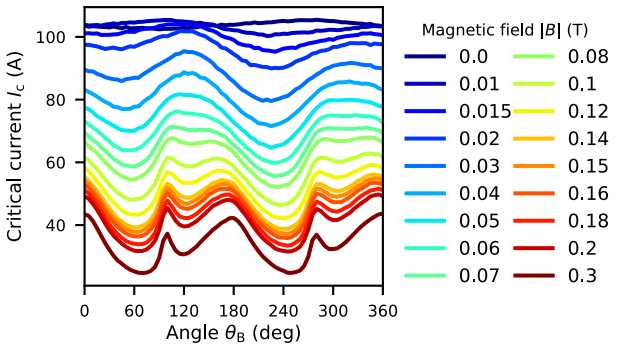


FIG. 4. measured, in-field $I_c(B, \theta)$ performance of 4 mm wide SuperPower SCS4050 AP superconductor, $I_c$ which we scaled to a 12 mm width as used in experiments.

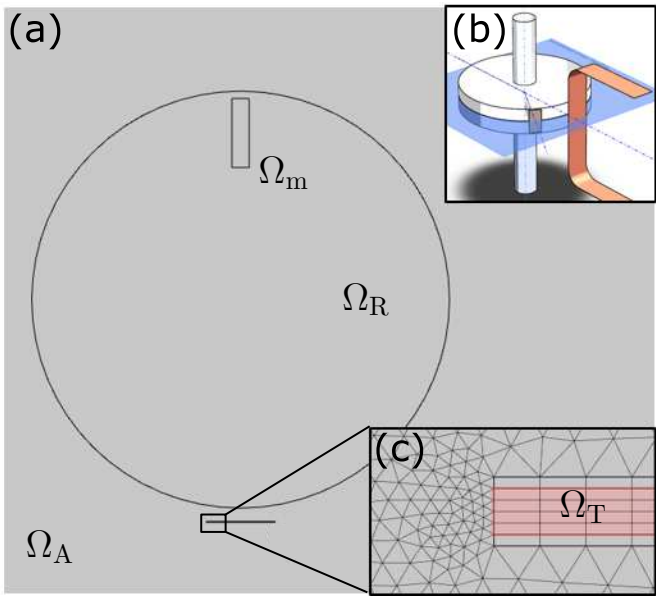


FIG. 5. (a) 2D model of the bisecting plane, with the Air $\Omega_A$, rotor $\Omega_R$, tape $\Omega_T$, and magnet $\Omega_m$ domains. (b) Inset showing a 3D schematic of the dynamo stator and rotor, and the modeled bisecting plane. (c) Magnified view of the Tape domain $\Omega_T$ and FE model mesh.

our problem to the 2D plane bisecting the stator and rotor. In this arrangement, shown in fig. 5(a), we define the $x$ axis to be oriented along the width of the tape, the $y$ axis along its thickness, and $z$ axis as out of plane.

The 12 mm wide superconducting layer is modeled as a 100 $\mu$m thick domain, rather than its real thickness of $\sim 1$ $\mu$m, this avoids the logarithmic singularity solutions for 2D conductors [43], and therefore improves convergences times [39, 44]. The copper stabilizer of the tape is modeled as two 25 $\mu$m , domains on the top and back surfaces of the superconducting domains. The resistivity of copper is assumed to be electrical grade, $\rho_{\mathrm{Cu}} = 0.19$ $\mu\Omega$cm.

In the $H$-formulation, the problem of solving Ampere's and Faraday's laws are expressed in terms of the electric field $\vec{E}$, the free current density $\vec{J}$, and the auxiliary field $\vec{H}$. This gives Ampere's law:

$$\nabla \times \vec{H} = \vec{J}, \tag{14}$$

and Faraday's law as:

$$\nabla \times \vec{E} = -d_t \vec{B}. \tag{15}$$

The finite element model is then constructed using edge elements [37], which assign the degrees of freedom of the model to the tangential component of the auxiliary field $\vec{H}$. This satisfies a weak form of stokes' theorem and defines $J_z$ explicitly by the tangential components of $\vec{H}$. This explicitly satisfies (14), and also enforces current continuity.

Equations 14 and 15 are then linked by the appropriate choice of constitutive relations. Firstly, the relation between the auxiliary and magnetic field:

$$\vec{B} = \mu_r \mu_0 \vec{H}, \tag{16}$$

where $\mu_r$ is the relative permeability, which is taken as 1. Secondly the relationship between current density and electric field:

$$\vec{E} = \rho \vec{J}, \tag{17}$$

where $\rho$ is the volumetric resistivity. To capture the behavior of the HTS material, we use the $E - J$ power law [45, 46]:

$$\rho = \frac{E_0}{J_c(|\vec{B}|, \theta_B)} \left| \frac{\vec{J}}{J_c(|\vec{B}|, \theta_B)} \right|^{n-1}, \tag{18}$$

where $E_0$ is the characteristic electric field, typically chosen as 1 $\mu$V/cm, $J_c(|\vec{B}|, \theta_B)$ is the critical current density, $\theta_B$ is the angle of the magnetic field with respect to the normal of the tape, and $n$ is the n-value which captures the steepness of the transition and is taken to be 20.

We take $J_c(|\vec{B}|, \theta_B)$ as measured experimentally in the SuperCurrent facility at Robinson Research Institute [47, 48], which is shown in fig. 4, and then normalize by the self-field critical current of the stator $I_c = 293$ A.

To solve the problem of representing a moving magnet inside the $H$-formulation formalism [49, 50], we represent the field of the magnet as a sheet current $J_m$ along the boundary $\partial\Omega_R$. To enforce this condition, we add a weak formulation condition to the finite element problem:

$$\nabla \times \vec{H} = J_m(\theta - \theta_{\mathrm{R}}(t)) \text{ on } \partial\Omega_R, \tag{19}$$

where $\theta$ is the azimuthal angle, and $J_m$ is rotated by $\theta_{\mathrm{R}}$ to simulate the rotation of the magnet.

To account for net transport currents $I_{\mathrm{T}}$ we consider the external power supply to be an ideal current source. Therefore we restrict the currents in the tape to obey:

$$I_{\mathrm{T}} = \int_{\Omega_T} \vec{J} \cdot d\vec{a} = \oint_{\partial\Omega_T} \vec{H} \cdot d\vec{l} \tag{20}$$

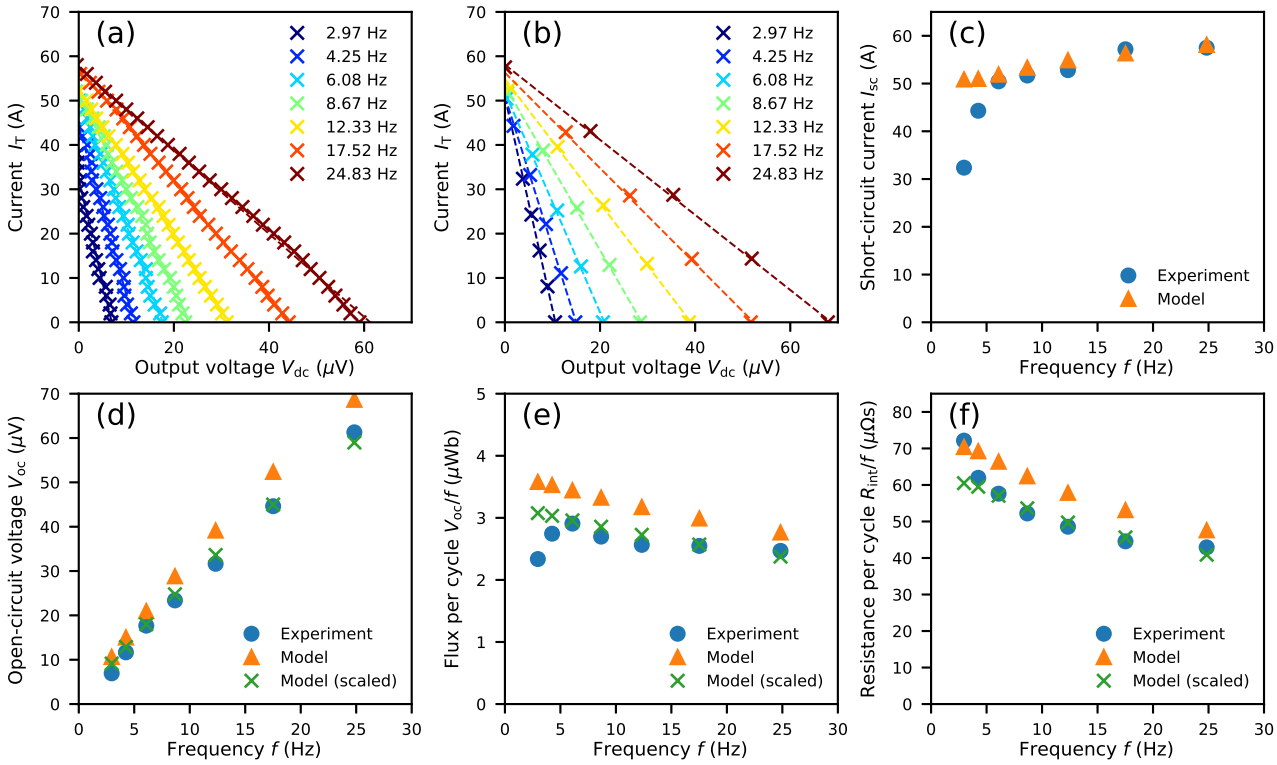


FIG. 6. Comparison of the DC electrical characterization of the HTS dynamo for experimental and modeled values. (a) Modeled, and (b) experimental $I$-$V$ characteristics for various frequencies. (c) Modeled and measured short-circuit current $I_{\rm sc}$ vs frequency. (d) Comparison of measured, modeled, and scaled open-circuit voltages $V_{\rm oc}$ vs frequency $f$. (e) Frequency normalized open-circuit voltage (flux per cycle) vs frequency. (f) Frequency normalized internal resistance $R_{\rm int}$ vs frequency.

Finally, the whole model is bounded on $\partial\Omega_A$, taken 300 mm away from the center, where $\hat{n} \times \vec{B} = 0$.

Each model is run for a total of 3 cycles, during the first cycle, the transport current is arbitrarily distributed but is redistributed by the applied magnetic field, which has some effect on the output. However on the second and third cycle the system is found to be periodic, and hence no further cycles are necessary. To capture the effect of frequency and transport current, we simply run the models with different rotational speeds of the shell current $J_m$ and different values for $I_{\rm T}$.

## V. RESULTS

First we present measured DC values which highlight that the model agrees with experiment over a large range of parameters, but do not test the local dynamics of the model directly.Next, transient electrical waveforms confirm that the model replicates the dynamics of the system. Finally, we present locally collected magnetic field data that confirms dynamic spatial agreement between the model and the experiment.

### A. DC characterization

The HTS dynamo can be characterized as a simple voltage source, as shown in fig. 1(b), with an open-circuit voltage $V_{\rm oc}$, an internal resistance $R_{\rm int}$, and a short-circuit current $I_{\rm sc}$. Figure 6 presents DC (time averaged) values from the electrical characterization of the experimental device and FE model. $I$-$V$ characteristics from the model, fig. 6(a), and experiment, fig. 6(b), are presented. From these $I$-$V$ characteristics, the key idealized parameters $V_{\rm oc}$, $V_{\rm oc}/f$, $I_{\rm sc}$, and $R_{\rm int}$ can be extracted, as shown in fig. 6(c) - (e) respectively.

Broadly speaking the model reproduces the $I$-$V$ behavior observed in experiment. At every frequency, the slope of the curves in fig. 6(a) and (b) is essentially linear, implying a constant internal resistance $R_{\rm int}$. And the magnitude of the values is clearly similar.

While the modeled $V_{\rm oc}$ includes a factor, $L$, from the extrapolation, see (13), the short-circuit current $I_{\rm sc}$ should not. That is, as we extrapolate the model from the 2D plane the amount of current is unaffected. Hence, fig. 6(c) provides the most stringent test of the model's accuracy. From this we see that the model reproduces the behavior extraordinarily well, with only a 5% deviation from the experimental values for the 5 highest frequencies. To eliminate the factor $L$, which is the only geomet-

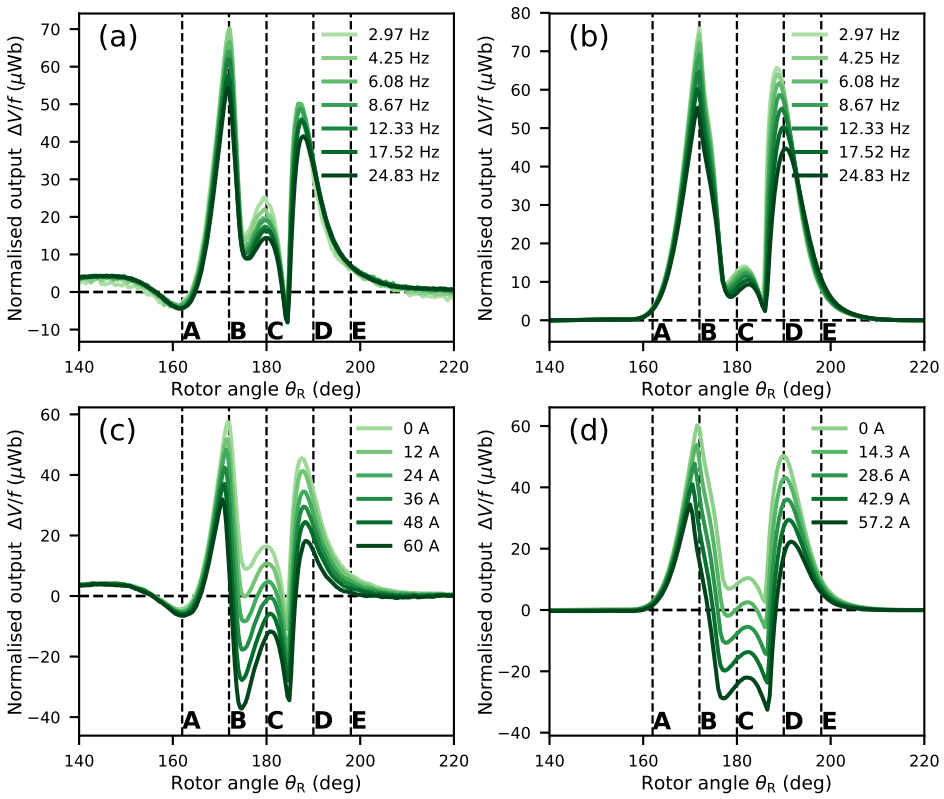


FIG. 7. Transient $\Delta V$ waveforms measured, left column, and modeled (scaled), right column. The points marked **A** to **E** match those defined in fig. 1(b). (a) and (b) show open-circuit frequency normalized $\Delta V$ vs rotor angle at several different frequencies. (c) and (d) show $\Delta V(I)$ waveforms for increasing transport current for 17.5 Hz.

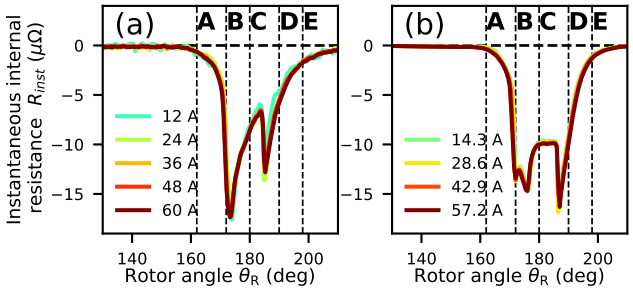


FIG. 8. Instantaneous resistance $R_{\mathrm{inst}}$ values vs rotor angle $\theta_{\mathrm{R}}$ for the transport currents reported in fig. 7 for (a) measured data, and (b) scaled models.

ric degree of freedom, we present a set of scaled values based on changing $L = 12.7$ mm in (13) to $L' = 10.2$ mm. This is done by fitting $V_{\mathrm{oc}}$ for the 5 matching frequencies from fig. 6(c). Note that $L' < L$ is expected given the divergence of the field in 3D. Figures 6(d-f) present both the the results from the raw model and the scaled values.

One of the most widely accepted behaviors of the HTS dynamos is the linear output dependence on frequency. This behavior is borne out in the models. Figure 6(d) compares the measured $V_{\mathrm{oc}}$ with the values extrapolated from the model, showing that while the unscaled model overestimates the output, the linearity is indeed reproduced. To examine the behavior more closely, fig. 6(e) normalizes the output voltages by the rotational frequency, exaggerating the deviations from the linear behavior. We can see that the experimental data shows a small scatter around what would be assumed to be a constant value, and hence an assumption of linearity is justified. This scatter is not present in the modeled data, showing a clear non-linear component.

A central question of the device is the nature of the internal resistance, and whether it can be appropriately described in the context of the dynamic resistance effects reported elsewhere [51, 52]. The scaled model and experimental data show tight agreement for the internal resistance of the device, including the downward trend in resistance per cycle for increasing frequency.

The interplay between $V_{\mathrm{oc}}$, $R_{\mathrm{int}}$, and $I_{\mathrm{sc}}$ highlights that the dynamo does not have some simple explanation via flux transfer across the stator tape. For example, the simplest flux transfer models would predict a constant flux

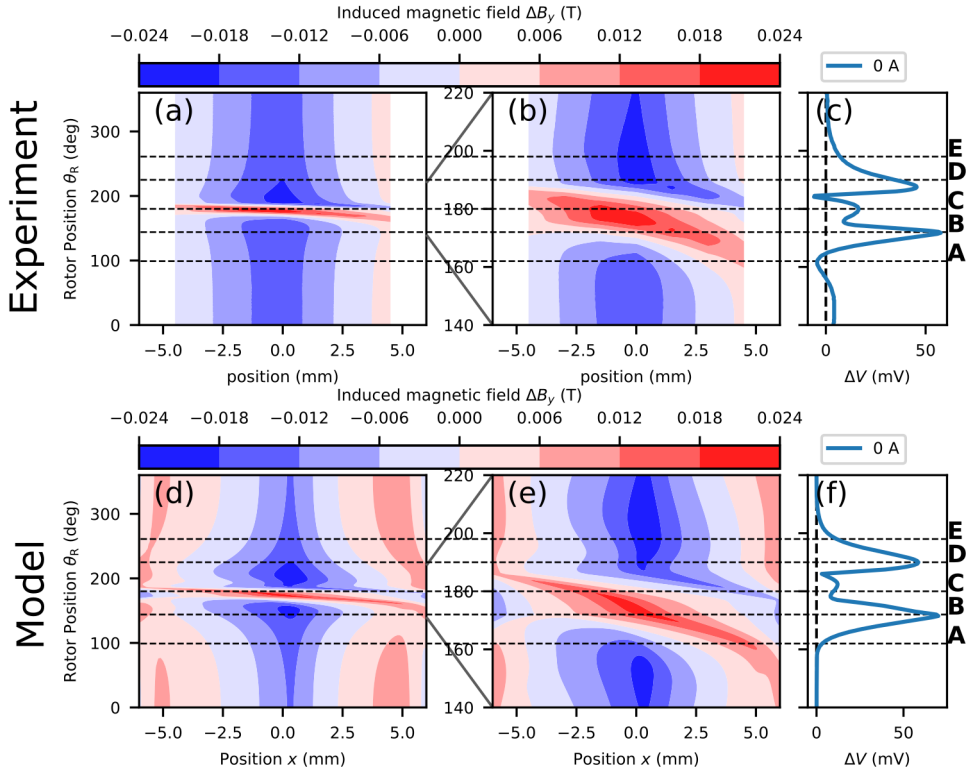


FIG. 9. Induced magnetic field $\Delta B$ across the width of the tape ($x$-axis) vs rotor angle $\theta_R$ ($y$-axis) at 17.52 Hz clockwise rotation (right to left). (a) Measured values from 7 Hall probes at 0.5 mm from the stator. (b) Zoomed view of (a). (c) Measured $\Delta V$ for (b). (d) Modeled data from full width of tape, at the same distance from the tape. (e) Zoomed view of (d). (f) Scaled $\Delta V$ for (e).

per cycle. This is even more interesting when considering that the internal resistance per cycle of the device not only drops — but drops faster than the flux transferred per cycle, as evidenced by the increasing $I_{sc}$ with frequency.

### B. Transient characterisation

The HTS dynamo is not a DC device, and transient behavior can be measured to test the model. Figure 7 shows several of the key $\Delta V$ waveforms from the scaled models and experiment. All the qualitative features are replicated in the transient behavior of the models. Furthermore, quantitative agreement is again achieved using the scaled value for $L'$, further indicating that no qualitatively important physical effects have been left out of the model.

Figures 7(a) and (b) show that, when normalised by frequency and plotted vs rotor position $\theta_R$, the open-circuit $\Delta V$ falls onto the same curve for all frequencies measured or modeled. The small deviations from linear scaling can be attributed to specific moments in the cycle. This indicates that while frequency has an effect, as shown in fig. 6, the effects are only small but systematic adjustments to a broadly similar behavior. Figures 7(a) and (b) show the key qualitative features of the HTS dynamo rectification, i.e., that it occurs primarily as the magnet enters $\mathbf{A} \rightarrow \mathbf{B}$, and exits $\mathbf{D} \rightarrow \mathbf{E}$. This is seen in the two dominant peaks. Figures 7(a) and (b) also show some important qualitative differences; fig. 7(a) has a clear lift as the magnet approaches and $\theta_R < 155^o$, this lift, and subsequent dip, are not present in the modeled value. This is the clearest example of how our approximation in (8) breaks down. However, the break down in the approximation does not obscure our ability to identify the dominant behaviors.

The appearance of the internal resistance can be seen in figs. 8(c) and (d), which show how each $\Delta V$ waveform changes with the increasing current through the stator. From these curves we can see that the dynamic resistance appears as a reduction in the output voltage waveform. Not only is this reduction localized to the voltage generating portion of the cycle, where the magnet is over the stator, but also seems to peel the waveforms away from each other at around point **B**. This peeling indicates that there is a portion of the cycle that does not experience the internal resistance, and that this portion reduces with increasing current. Furthermore, changes in the middle of the wave forms between $\mathbf{B} \rightarrow \mathbf{D}$ clearly indicate that the initially (open-circuit) low output during these times is not due to a lack of dynamics, but rather coincidental

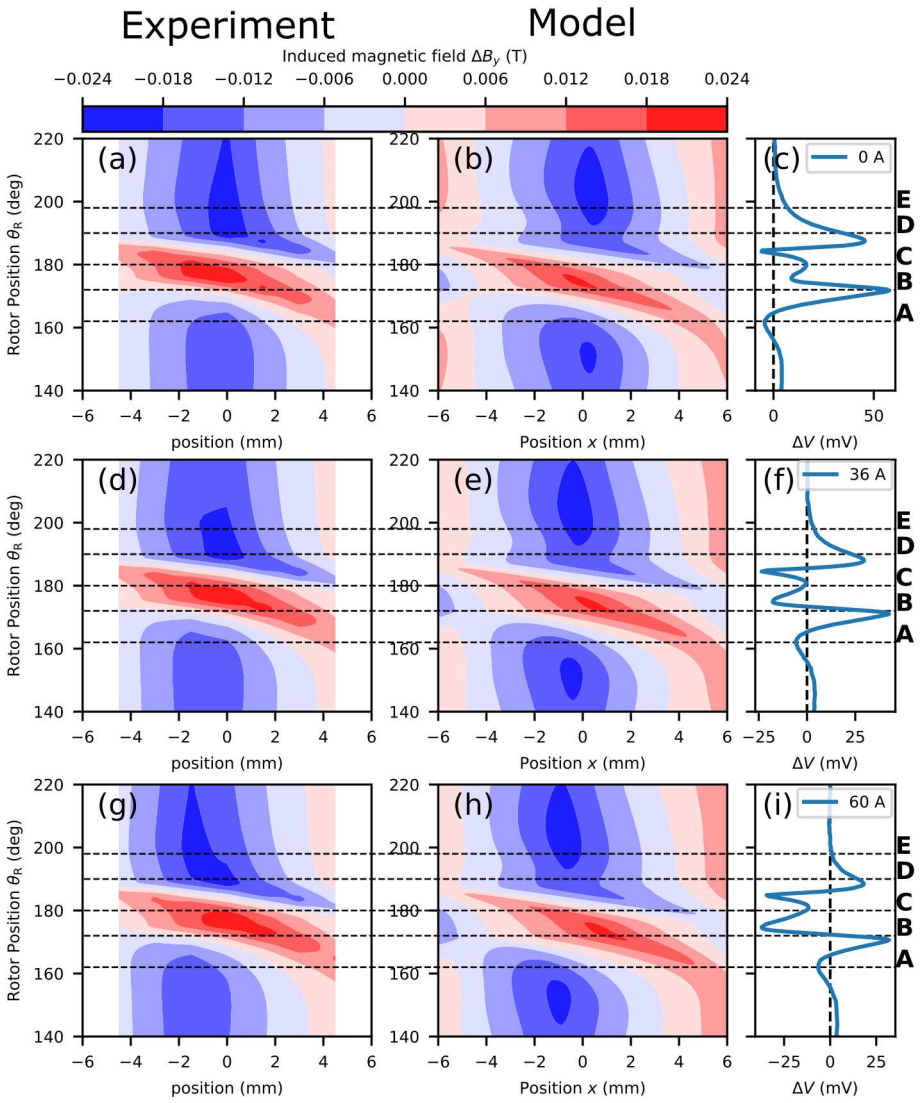


FIG. 10. Induced magnetic field $\Delta B$ position along tape width $x$ and rotor angle $\theta_{\mathrm{R}}$ contour plots for measured and modeled values at several net transport currents for 17.52 Hz clockwise rotation (right to left). (a), (b) Measured and modeled $\Delta B$ respectively at $I_{\mathrm{T}} = 0$. (c) Measured $\Delta V$ at $I_{\mathrm{T}} = 0$. (d), (e) Measured and modeled $\Delta B$ respectively at $I_{\mathrm{T}} \approx 0.5 I_{\mathrm{sc}}$. (f) Measured $\Delta V$ at $I_{\mathrm{T}} \approx 0.5 I_{\mathrm{sc}}$. (g), (h) Measured and modeled $\Delta B$ respectively at $I_{\mathrm{T}} \approx I_{\mathrm{sc}}$. (i) Measured $\Delta V$ at $I_{\mathrm{T}} \approx I_{\mathrm{sc}}$

to the lack of transport current.

A further question regarding the internal resistance is its apparent constant value for any given current and fixed frequency. This could simply be a coincidence, hidden by the DC time average used in fig. 6. To avoid this we introduce the instantaneous resistance:

$$R_{\mathrm{inst}} = \frac{V_{77\mathrm{K}}(I,t) - V_{77\mathrm{K}}(0,t)}{I} \tag{21}$$

$$= L' \frac{E_{\mathrm{ave}}(I,t) - E_{\mathrm{ave}}(0,t)}{I}. \tag{22}$$

Figure 8 shows (a) the measured and (b) modeled values of $R_{\mathrm{inst}}$ vs magnet position during each cycle. All curves follow the same non trivial shape, just as the frequency scaled open-circuit voltages in fig. 7(a) collapsed on each other. While we see some deviations between the model and experiment, again we attribute this to a breakdown in our approximation (8), and note that the amount of diamagnetically shielded flux must therefore be highly systematic.

### C. Magnetic field

While DC values are critical for operational predictions, and transient behaviors allow us to confirm the behavior without the DC time average, all the results presented so far are obscured by the spatial averaging effect of comparing $\Delta V$ with $E_{\mathrm{ave}}$, see (11). Ultimately, $E_{\mathrm{ave}}$ is the result of the spatial dynamics of the over-currents inside the stator. Therefore, if claims are to be made as to the effects of the spatial distributions of these currents,

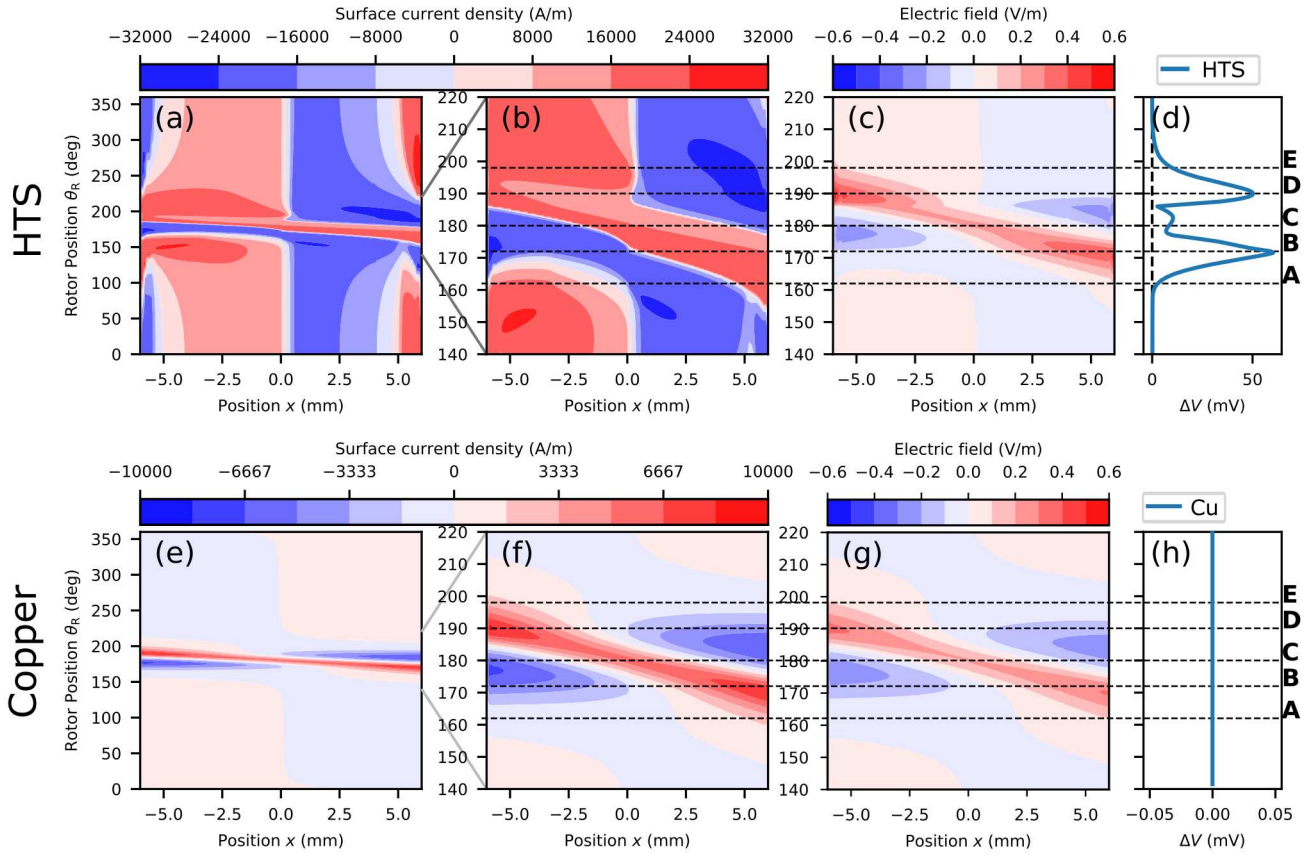


FIG. 11. Modeled sheet current densities, electric field in the superconducting (a)-(d) and normal (e)-(h) stators vs position across the width of the tape $x$ and rotor angle $\theta_R$ for 17.52 Hz clockwise rotation (right to left) in open-circuit. (a), (e) Sheet current density for full cycle. (b), (f) Zoomed view of the sheet current density for the magnet's transit. (c), (g) Zoomed view of the local electric field $E_z$ in the sheet. (d), (h) corresponding plot of modeled $\Delta V$ equal to zero for copper. Dashed lines highlight key magnet positions.

then the model's spatial degrees of freedom need to be tested against experiment.

Figure 9 compares experimental and modeled values for the magnetic field difference $\Delta B$, defined in (5), for $f$ =17.52 Hz (clockwise rotation). This is perpendicular to the stator's surface and taken along a line across the width of the stator and 0.5 mm behind it, as shown in Figure 3. In the case of the experimental data, the contour plots linearly interpolate the values in between the 7 sensors of the array. For the model itself, the data is taken along a line, 0.5 mm from the tape's back edge, and is plotted as is. The $x$ axis of the contours corresponds to the $x$ position along the width of the tape, whereas the $y$ axis is used to denote the angle of the rotor $\theta_R$. Figure 9 shows the full cycle of the dynamo, which is dominated by the remnant magnetisation as the over-currents relax under flux creep. Here we see the largest disagreement between the model and experiment, with the remnant magnetisation profiles being strikingly different. However, the aim of the model is not to reproduce the flux creep effects in these devices, and the $n$-index was set at 20 as models appeared insensitive to its value.

Figure 10 presents $\Delta B$ for the 17.52 Hz data, zooming in to focus on the induced magnetic field during the magnet's transit, for several different values of the net transport current $I_T$. We see excellent agreement between the model and the experiment during the dynamics of the magnet's transit over the tape. Inspecting fig. 10 further, we can identify several features during the transit. We can see the magnet enter from the right hand side of the plot, as the induced current precedes the applied magnetic field. As the magnet travels across the conductor, these shielding currents erase the remnant magnetization in the conductor. As the magnet leaves, this remnant magnetization reasserts itself, with a characteristic jump in intensity between **D** and **E**, as the magnetic field suppression of $J_c(|\vec{B}|, \theta_B)$ subsides. Finally, with the magnet clear of the conductor, we see a slow decay of these currents into the final remnant magnetization.

Looking at fig. 10, notice that the response is almost unchanged with the addition of transport current. The easiest way to identify that there is a change at all is to focus on the center of the remnant magnetization as it shifts to the left. Spanning the $I$-$V$ characteristic of the

device, from $I_{\rm T} = 0$ to $I_{\rm T} = I_{\rm sc}$, we see essentially no change in the shielding behavior of the device. And yet, the $\Delta V$ waveforms in figs. 10(c) and (f) clearly capture the reduction in output voltage.

Ultimately it is our goal to reconstruct the dynamics of the device, which are determined by the dynamics of the underlying current flows $\vec{J}$. As $\Delta B$ is the induced magnetic field from those currents, we can make the desired conclusions from the calculated current density $\vec{J}$ with some certainty given a correspondence between the measured and modeled values of $\Delta B$.

### D. Current maps

Figure 11 shows several contour plots constructed similarly to fig. 9 of the current densities flowing through the tape at each part of the cycle for both HTS and copper stators. Note that the current density here is the sheet current density defined by:

$$K_z = \int_h J_z dy, \tag{23}$$

where, $h$ is the thickness of the tape. During the transit of the magnet, the current density in the HTS is significantly higher than the critical current of the tape, $J_z > 1.5 J_{\rm c}$. This correlates with the fact that the measured voltages imply that the stator has been driven considerably far into the flux flow regime. It also implies that the real device has a significantly different current distribution to any prediction using Bean's critical state model which would limit $J_z \leq J_{\rm c}$. In contrast, the current distribution in the copper, figs. 11(e) and (f), is simply a scaled multiple of the local *emf* fig. 11(g). Given the similarity between the *emf* in the HTS ( fig. 11(c)) and copper ( fig. 11(g)), we can also conclude that the stator dynamics are dominated by the applied magnetic field for the majority of the magnet's transit. As the conductor is primarily in the flux flow regime, the shape of the electric field is essentially set by the rate of change of the applied magnetic field, via Faraday's law.

The source of the small difference between the *emf* in the copper and the HTS ( fig. 11(c) and (g) respectively ) can be seen by examining the current densities figs. 11(b) and (f). From this we see why it is that the HTS dynamo is capable of generating a non-trivial $E_{\rm ave}$. That is, at every moment of the cycle, the current densities must sum to the total transport current, in this case $I_{\rm T} = 0$. However, as the HTS is driven by the applied *emf* it is not constrained to average to zero, as in the normal conductor, figs. 11(e) and (f).

Locally speaking the output *emf* of the dynamo, as a source of electrical energy for a connected load, must be associated with the eddy current underneath the magnet (the red forward current that transitions from right to left), as it has the correct polarity. We can also note that the device is also fundamentally dissipative: no currents ever experience a negative power i.e. $E.J \not< 0$. Note that

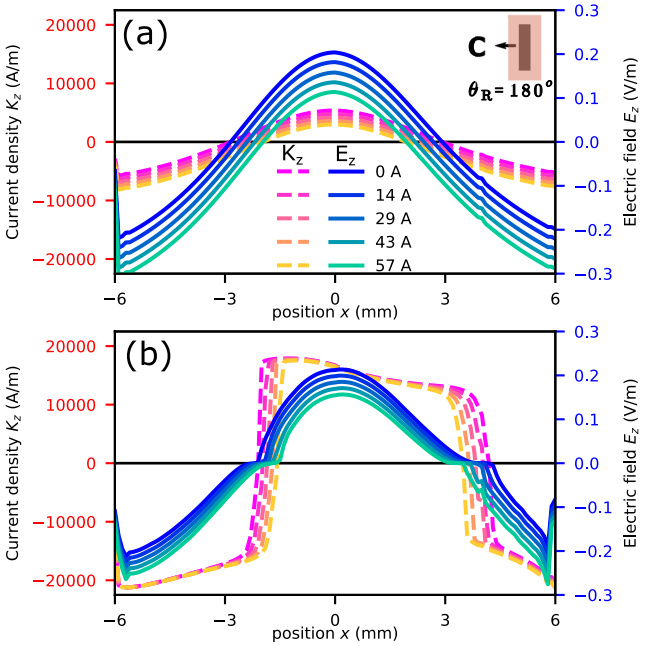


FIG. 12. Current (dashed lines) and local electric field (solid lines), from $I_{\rm T} = 0$ (dark shades) to $I_{\rm T} = I_{\rm sc}$ (light shades) vs position across the width of the tape $x$, for copper (a) and HTS (b) at rotor position **C**. Data presented for 17.52 Hz. Magnet position is illustrated as viewed from the Hall array.

the output of the device naturally drives current in the backward direction.

Further inspection of fig. 11(c) shows that the magnet continues to provide the desired *emf* for the entire transit, as one would have predicted from a normal spot/flux transfer model in the LTS case. However, unlike the the LTS dynamo, the current under the magnet as it transits is considerably larger, and must return in order to maintain the current constraint. It is this return current that both reduces the output between **B** and **D**, but also becomes the driven current $I_{\rm T}$.

Figure 12 shows a snapshot of the current and electric field distributions across the width of the tape, for copper and HTS, at position **C** in the cycle for varying net transport currents. For copper, fig. 12(a), we see the expected curves, where the positive peak electric field is under the magnet, and the current densities are simply scaled versions of the electric field profile. For increasing currents, the current distributions in copper shift uniformly downward, resulting in the expected resistive $E_{\rm ave}$. For HTS we observe that the shape of $E_z$ is broadly similar for each current, (as well as to copper), again reinforcing that the shape of the electric field is predominantly determined by the applied magnetic field via Faraday's law. Unlike copper, increasing net currents $I_{\rm T}$ are achieved by shifting the turning points of the current distribution $J_z$ inward. However, the effect of changing the position of the current turning points, combined with the observation that the shape of $E_z$ is broadly similar each time, leads to the simple conclusion that the average

electric field is whatever it needs to be in order to satisfy the current constraint on the system. Therefore the internal resistance of the HTS dynamo corresponds to a reallocation of the applied local *emf* from the the driving direction (forward eddy current under the magnet) to the output direction (return eddy currents around the magnet).

Figures 13(a), (b), and (c) show how the eddy currents redistribute in order to accommodate the transport current $I_{\mathrm{T}}$ at three different positions along the $I$-$V$ characteristic, matching the $\Delta B$ plots presented in fig. 10. Here it is useful to distinguish between eddy currents driven by the magnet, and the remnant magnetization currents that these eddy currents relax into after position **E**. If we focus on rotor positions before the magnet's transit, the transport current is asymmetric with respect to the forward and backward remnant currents, which is similar to the case of the dynamic resistance. As the magnet enters at **A**, the remnant current, including the transport current, is pushed to the right of the conductor, and we see the forward eddy current under the conductor makes its way across the width. The fact that there is no location in the conductor where the current does not at some point flow in the backward direction distinguishes this situation from simple dynamic resistance.

Increased transport current displaces the forward remnant current shown in red. Because this system is cyclical, and the current is kept constant, the competition (loss) between the transport current and remnant current is not apparent at the start of the cycle. Secondly, we see that the backward eddy current underneath the magnet decreases in size (as a fraction of conductor width) as the transport current is increased, which can also be seen in fig. 12. This decrease in size reduces the amount of the applied *emf* that is captured in the driving direction, and instead we see it picked up in the backward direction as transport dissipation or $R_{\mathrm{int}} \times I_{\mathrm{T}}$.

As we have previously noted from fig. 7, the internal resistance does not appear uniformly across the cycle. Instead, we can see parts of the cycle that experience very little dynamic resistance. This can be inspected by following the dashed line for **B** through all the plots in fig. 13, where we see that the sharp increase in the dynamic resistance corresponds with the elimination of sub-critical currents in the stator. Once the stator is full with over-critical current, the competitive effect between the forward and backward eddy currents leads to the internal resistance. This leads to the conclusion that there is some other smaller mechanism to the internal resistance that is in play before **B**.

To examine this, fig. 14 shows the sheet current and electric field, for both copper and HTS, when the rotor is halfway between positions **A** and **B**, denoted $\mathbf{A}^{+}$, across the whole $I$-$V$ curve. For copper, fig. 14(a), we see the effect of the magnet entering from the right and currents returning on the left, with a uniform shift up the y-axis for increasing $I_{\mathrm{T}}$. In complete contrast fig. 14(b) shows that , the current distribution in the HTS accommodates the additional $I_{\mathrm{T}}$ by broadening in the x-axis direction, thus 'filling' in the sub-critical region on the left hand side of the stator. This leaves the local *emf* from the applied magnetic field unchanged with current. It is clear from fig. 13(d) that there should be some small internal resistance at this position, which can be identified with the smaller electric field lobe (identified by the blue arrow in fig. 14(b)) in the center of the tape. This smaller lobe of the electric field corresponds to the remnant magnetization being forced out of the tape, and constitutes a completely different resistive mechanism to the one seen between positions **B** and **D**.

## VI. DISCUSSION

### A. Origin of the DC voltage $V_{\mathrm{oc}}$

The arguments presented here revolve around 3 equations (15), (18), and (20) and how they interact to give $E_{\mathrm{ave}}$. While it is absolutely true that the $A$-vector must be cyclical in these conditions, the currents that flow in response to the local electric field can give rise to non trivial solutions for $\vec{\nabla}\psi$. By examining fig. 12 we can see that the shape of the electric field is essentially the same regardless of transport current, only shifting up and down to match the current constraint. This phenomenon is fundamentally different to the equivalent conventional dynamo, where the current constraint also maintains zero voltage. However, this story doesn't hold when there are still sub-critical regions of the tape. When there is still room for transport current to displace sub-critical currents, the penetrated magnetic field only contributes to the driving direction (forward current under the magnet). This situation is likely much more similar to the normal spot operation seen in the LTS dynamos [53], where the penetrated flux can migrate in penetrated normal zones.

The mechanism here should have some bearing on the mechanism of the other flux pumps. For the HTS rectifier-type flux pumps Geng et. al. [19] give an explanation in terms of flux linkage and the movement of the electric central line. As the HTS rectifier is based on a dynamic resistance switch to rectify an applied AC emf, the movement of the electric field central line is very much akin to the movement of the electric field distributions in fig. 12. The situation in the dynamo is of course complicated by the fact that the applied *emf* and the rectifying *emf* are one and the same. What does not have an analogue in the model by Geng et. al. is the secondary resistive or generative mechanism highlighted in fig. 14. In the rectifier, the only way to link the applied flux into the load is to create the kind of current competition we see between positions **B** and **D**.

As for understanding the device using macroscopic flux-coupling, as proposed by Wang et. al [34], we find no evidence that the results presented here require any new physics. Two major points support this: A) the work in Wang et. al. is in a rotationally symmetric sys-

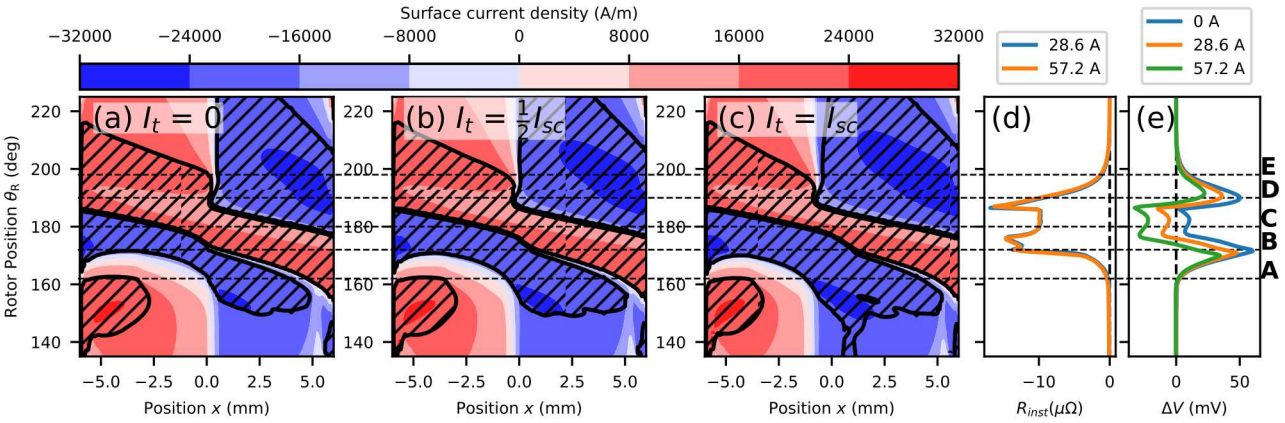


FIG. 13. Modeled current contours vs $R_{\rm inst}$ and $\Delta V$ for several currents at 17.52 Hz, cross-hashed regions identify $J > J_{\rm c}$. (a) $I_{\rm T} = 0$. (b) $I_{\rm T} = 1/2 I_{\rm sc}$. (c) $I_{\rm T} = I_{\rm sc}$. (d) $R_{\rm inst}$. (e) $\Delta V$.

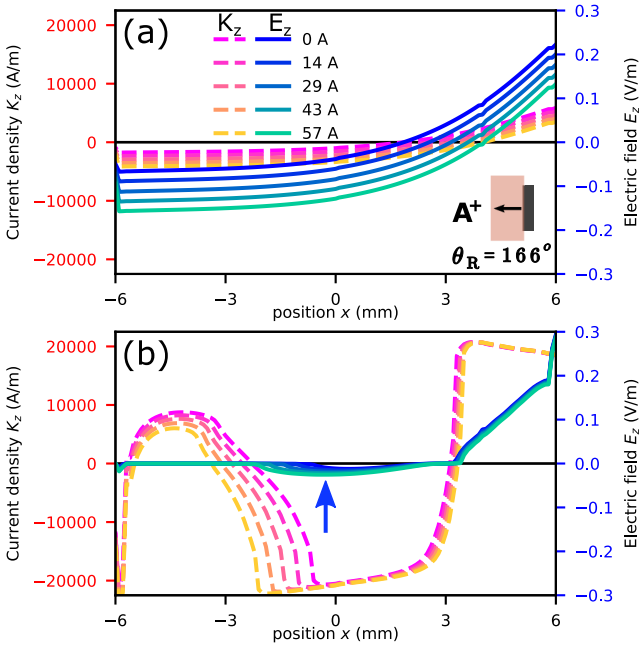


FIG. 14. Sheet current density $K_z$ (dashed lines) and local electric field $E_z$ (solid lines), along the 17.5 Hz $I$-$V$ curve from $I_{\rm T} = 0$ (dark shades) to $I_{\rm T} = I_{\rm sc}$ (light shades) vs position across the width of the tape $x$, taken for the rotor position $\mathbf{A}^+$, halfway between positions $\mathbf{A}$ and $\mathbf{B}$, $\theta_{\rm R} = 166^o$. Data presented for 17.52 Hz. Magnet position is illustrated as viewed from the Hall array.

tem where the azimuthal voltage can not be defined, let alone adapted to results for the dynamo. B) the results presented in Wang et. al. do not use a $J_{\rm c}(|\vec{B}|, \theta_B)$ function and so the equations solved can not be affected by the DC offset of the magnetic field as claimed by the authors. Even if this was disputed, our results in [12] clearly show that the DC voltage can be achieved by a system with zero DC magnetic field sensitivity.

### B. Output voltage vs current, $R_{\rm int}$ vs $V_{\rm oc}$

The first major success in understanding the HTS dynamo was in capturing the frequency and magnetic field dependence of the internal resistance [3]. This was done by conceptualizing the internal resistance as a DC dynamic resistance, akin to what is seen with DC transport currents in purely oscillatory magnetic fields [51]. To explain the rest of the $I$-$V$ curves, given the gradient of the curve $R_{\rm int} = R_{\rm dyn}$, we have two options for the additional physics, to fix $I_{\rm sc}$ as some fundamental property of the system, or relate $V_{\rm oc}$ to $R_{\rm int}$ via some underlying mechanism.

As argued in sec V D, we see that the internal resistance is generated by competition between the transport current and the driven eddy current. Figure 12 shows that the shape of electric field is largely unchanged by $I_{\rm T}$. Rather we argue that $\partial_z \psi$ is determined at any given time to be the shift of $E_z$ that solves (20). Therefore, we must conclude that the correct interpretation is that $V_{\rm oc}$ and $R_{\rm int}$ must be understood with respect to the same underlying mechanism that generates $E_{\rm ave}$ in general. Although, this is not true before psotion **B**, as seen in fig. 14, where the resistive mechanism is related to the movement of remnant magnetisation rather than a reallocation of the applied *emf*. This secondary smaller mechanism is again similar to that described by Mawardi [54] in the LTS dynamos.

### C. Short-circuit current $I_{\rm sc}$

Given the relationship between $R_{\rm int}$ and $V_{\rm oc}$, we see that $I_{\rm sc}$ is not a fundamental parameter of the system. In fact this behavior makes sense with respect to the definition of $I_{\rm sc}$ used here, where it is a DC property of an otherwise dynamic device. Nothing particularly special happens at any given moment of the cycle when $I_{\rm sc}$ is flowing through the tape. Rather $I_{\rm sc}$ simply happens

to be the current where the time average of the output happens to be zero. If one considers a dynamic definition of $I_{\rm sc}$, using a voltage rather than current control, one then naturally asks what the relationship between this dynamic and the DC short-circuit currents would be.

While we leave this point for future work, it does highlight that we would expect the load reactance to play some role in the rectification effect. This also explains the experimental results presented here in fig. 6 for the two lowest frequencies 2.97 and 4.25 Hz, where the electronic load has an insufficient inductance to oppose the small changes in net current driven by the magnet as it passes the stator at a relatively slow speed. We also take the view that in fig. 6(c) the trend must approach zero at zero frequency, as the plot will invert to the opposite polarity as the rotational direction is inverted, a behavior the experimental data here seems to bear out. This does provide some motivation for a model with an inductive boundary condition, rather than the infinite reactance used here. Ultimately, most practical magnets will have an inductance suitably high to appear essentially infinite to the dynamo.

### D. Resistivity vs current

One of the primary observations of the reported HTS dynamos is their linear $I$-$V$ characteristic. In complex systems, something can be linear for two reasons: A) the underlying mechanism is linear, and superposition maintains the linearity in the emergent behavior, or B) the effect in question is only interrogated over a small part where it appears linear. In the case of the HTS dynamo, it is safe to say the underlying behavior is not linear, and therefore case A can be rejected.

We must conclude that the dynamos built so far only explore a small portion of some underlying behavior. We have shown here for example that the internal resistance is not only constant in the DC values, but also when expressed instantaneously at every moment of the cycle. However, the difference in the behavior of the device between open-circuit and closed circuit is very small. In fact, the qualitative behavior of the device is the same for all the currents. If we focus on fig. 12 we can see that shape of the electric field across the width of the conductor is unaffected by the introduction of transport current. Consider how this curve moves, upward or downward, which corresponds to a change in the output voltage $\partial_z \psi(t)$. We can see that it is the gradient of the applied magnetic field, at the turning points of the current, that determine the change in voltage for a given change in current.

Figure 13 shows that the turning points of the sheet current $K_z$ do not change all that drastically over the $I$-$V$ curve of the device. That is to say, the dynamo only explores a small section of the applied local-*emf*, when deciding its turning points. Hence, while the overall output of the device is a function of the total applied local-*emf*, the behavior when changing the current only samples the applied-*emf* at the locations of the turning points. Therefore, when changing the current, only a small section of the local-*emf* is explored, over which it must appear linear.

To further test this, we propose experiments using far wider stators than those explored so far, or to use parallel stators to create multiple return paths. Wider stators can carry more current over all, broadening the space over which the turning points in the current can be pushed. For sufficiently large/high-current stators we would expect a non linear $I$-$V$ characteristic, as the local-*emf* is probed at different locations[55].

### E. Partial magnetic field penetration

The second behavior that prompts us to suggest wider stators is the observation that for some part of the cycle the internal resistance is an order of magnitude lower even while generating rectified output. This can be seen in fig. 7, and by inspecting the instantaneous resistance in fig. 8 between $\mathbf{A} \rightarrow \mathbf{B}$. First we observe the fact that the applied magnetic field fully penetrates the whole tape for most of the magnet's transit. However, this is a geometric effect; a sufficiently wide stator would always have some region that was in the shielded regime. Or parallel stators could act as return paths while not under a magnet. We see that the internal resistance effect when displacing remnant magnetization is quite different to that when the transport current is competing with the driven eddy currents. While the output $E_{\rm ave}$ at the start of the transit is unaffected by increasing transport current, the loss associated with the competition between magnetization currents and transport current is likely seen in the tail of the internal resistance past **E**, see fig. 8. That is, as the driven eddy currents relax into the remnant magnetization, the presence of transport current reduces the output. If this mechanism results in a significantly lower drop in $\Delta V$, then large stators should have significantly improved short-circuit currents for a given magnet geometry.

## VII. CONCLUSION

A predictive and powerful model of the HTS dynamo has been presented, validated against experiments and interrogated. The agreement between the model and the experimental data clearly indicates that inclusion of the non-linear $E$-$J$ characteristics of the HTS film has a profound effect. This non-linearity gives rise to the DC voltage, as it breaks the oft overlooked symmetry in eddy current effects which is given by Ohm's law. The effects of this are seen at several levels of the analysis: DC quantities, transient voltage waveforms, and locally measured induced magnetic field distributions.

The model's dynamics can be interrogated for insights into their driving principles. Here we have outlined how the local applied magnetic field across the HTS stator is rectified by the non-linear *E*-*J* characteristic of the HTS material in the flux flow regime. Furthermore, we have shown that the link between this rectified output and the transport current through the stator is predominantly caused by the competition between the transport current and the driven eddy current caused by the magnet's transit.

Finally, we identify a partially-critical regime where the stator is only partially penetrated by the applied magnetic field. While we attribute a small resistance to the competition between the transport current and magnetization currents in this regime, this resistive mechanism is much smaller than when the stator is fully penetrated by the applied magnetic field. Logically we conclude that much lower internal resistances can be achieved by increasing the stator width sufficiently that the stator is never fully penetrated during the cycle of the device.

## ACKNOWLEDGMENT

The authors would like to thank Dr. Stuart Wimbush for providing $J_c$ data for the SuperPower tape. The Authors would like to acknowledge financial support from New Zealand MBIE Endeavour grant no. RTVU1707, and NZ Royal Society Marsden Grant no. MFP-VUW1806. M.A. acknowledges financial support from an EPSRC Early Career Fellowship EP/P020313/1.

[1] C. Hoffmann, D. Pooke, and A. D. Caplin, IEEE Trans. Appl. Supercond. **21**, 1628 (2011).
[2] T. A. Coombs, J. F. Fagnard, and K. Matsuda, IEEE Trans. Appl. Supercond. **24**, 8201005 (2014).
[3] Z. Jiang, K. Hamilton, N. Amemiya, R. A. Badcock, and C. W. Bumby, Appl. Phys. Lett. **105**, 112601 (2014).
[4] J. Geng and T. A. Coombs, Appl. Phys. Lett. **107**, 142601 (2015).
[5] J. Geng, B. Shen, C. Li, H. Zhang, K. Matsuda, J. Li, X. Zhang, and T. A. Coombs, Appl. Phys. Lett. **108**, 262601 (2016).
[6] J. Geng, K. Matsuda, L. Fu, J.-F. Fagnard, H. Zhang, X. Zhang, B. Shen, Q. Dong, M. Baghdadi, and T. A. Coombs, J. Phys. D **49**, 11LT01 (2016).
[7] C. W. Bumby, Z. Jiang, J. G. Storey, A. E. Pantoja, and R. A. Badcock, Appl. Phys. Lett. **108**, 122601 (2016).
[8] C. W. Bumby, R. A. Badcock, H.-J. Sung, K.-M. Kim, Z. Jiang, A. E. Pantoja, P. Bernardo, M. Park, and R. G. Buckley, Supercond. Sci. Technol. **29**, 024008 (2016).
[9] S. Lee, W. Kim, Y. Kim, J. Lee, S. Park, J. Lee, G. Hong, S. Kim, J. Han, Y. J. Hwang, and K. Choi, IEEE Trans. Appl. Supercond. **26**, 0606104 (2016).
[10] A. M. Campbell, Supercond. Sci. Technol. **30**, 125015 (2017).
[11] K. Hamilton, A. E. Pantoja, J. G. Storey, Z. Jiang, R. A. Badcock, and C. W. Bumby, IEEE Trans. Appl. Supercond. **28**, 5205705 (2018).
[12] R. C. Mataira, M. D. Ainslie, R. A. Badcock, and C. W. Bumby, Appl. Phys. Lett. **114**, 162601 (2019), https://doi.org/10.1063/1.5085226.
[13] A. Ghabeli and E. Pardo, Supercond. Sci. Technol. **33**, 035008 (2020).
[14] C.-S. Lee, B. Jankó, I. Derényi, and A.-L. Barabási, Nature **400**, 337 (1999).
[15] M. P. Oomen, M. Leghissa, G. Ries, N. Proelss, H. . Neumueller, F. Steinmeyer, M. Vester, and F. Davies, IEEE Trans. Appl. Supercond. **15**, 1465 (2005).
[16] T. Nakamura, M. Sugano, T. Doi, and N. Amemiya, IEEE Trans. Appl. Supercond. **20**, 1033 (2010).
[17] Z. Bai, C. Chen, Y. Wu, and Z. Zhen, Cryogenics **51**, 530 (2011).
[18] W. Wang, F. Spaven, M. Zhang, M. Baghdadi, and T. Coombs, Appl. Phys. Lett. **104**, 032602 (2014).
[19] J. Geng and T. A. Coombs, Supercond. Sci. Technol. **31**, 125015 (2018).
[20] J. D. D. Gawith, J. Ma, B. Shen, C. Li, J. Yang, Y. ztrk, and T. A. Coombs, Supercond. Sci. Technol. **32**, 095007 (2019).
[21] A. He, C. Xue, and Y.-H. Zhou, Applied Phys. Lett. **115**, 032602 (2019).
[22] J. Geng, C. W. Bumby, and R. A. Badcock, Supercond. Sci. Technol. (2020).
[23] K. S. Haran, S. Kalsi, T. Arndt, H. Karmaker, R. Badcock, B. Buckley, T. Haugan, M. Izumi, D. Loder, J. W. Bray, P. Masson, and E. W. Stautner, Supercond. Sci. Technol. **30**, 123002 (2017).
[24] C. Hoffmann, R. Walsh, E. Karrer-Mueller, and D. Pooke, Physics Procedia **36**, 1324 (2012).
[25] R. M. Walsh, R. Slade, D. Pooke, and C. Hoffmann, IEEE Trans. Appl. Supercond. **24**, 4600805 (2014).
[26] S. L. Wipf, Proceedings of the 1968 Summer Study On Superconducting Devices and Accelerators , 632653 (1968).
[27] O. Mawardi, A. Gattozzi, and H. Chung, IEEE Transactions on Magnetics **15**, 828 (1979).
[28] S. Kalsi, *Applications of High Temperature Superconductors to Electric Power Equipment* (Wiley-Blackwell, 2011) Chap. 3, pp. 35–58.
[29] H. W. Weijers, W. D. Markiewicz, A. J. Voran, S. R. Gundlach, W. R. Sheppard, B. Jarvis, Z. L. Johnson, P. D. Noyes, J. Lu, H. Kandel, H. Bai, A. V. Gavrilin, Y. L. Viouchkov, D. C. Larbalestier, and D. V. Abraimov, IEEE Trans. Appl. Supercond. **24**, 4301805 (2014).
[30] D. X. Ma, S. Matsumoto, R. Teranishi, T. Ohmura, T. Kiyoshi, A. Otsuka, M. Hamada, H. Maeda, Y. Yanagisawa, H. Nakagome, and H. Suematsu, Supercond. Sci. Technol. **27**, 085014 (2014).
[31] J. Ma, J. Geng, J. Gawith, H. Zhang, C. Li, B. Shen, Q. Dong, J. Yang, J. Chen, Z. Li, and T. A. Coombs, IEEE Trans. Appl. Supercond. , 8663420 (2019).
[32] J. Geng and M. Zhang, Supercond. Sci. Technol. **32**, 084002 (2019).

[33] M. Faraday, Phil. Trans. R. Soc. Lond **122**, 125 (1832).
[34] W. Wang and T. Coombs, Phys. Rev. Applied **9**, 044022 (2018).
[35] K. Kajikawa, T. Hayashi, R. Yoshida, M. Iwakuma, and K. Funaki, IEEE Trans. Appl. Supercond. **13**, 3630 (2003).
[36] Z. Hong, A. M. Campbell, and T. A. Coombs, Supercond. Sci. Technol. **19**, 1246 (2006).
[37] R. Brambilla, F. Grilli, and L. Martini, Supercond. Sci. Technol. **20**, 16 (2006).
[38] M. D. Ainslie, T. J. Flack, and A. M. Campbell, Physica C **472**, 50 (2012).
[39] M. D. Ainslie, C. W. Bumby, Z. Jiang, R. Toyomoto, and N. Amemiya, Supercond. Sci. Technol. **31**, 074003 (2018).
[40] R. A. Badcock, S. Phang, A. E. Pantoja, Z. Jiang, J. G. Storey, H. Sung, M. Park, and C. W. Bumby, IEEE Trans. Appl. Supercond. **27**, 5200905 (2017).
[41] A. E. Pantoja, Z. Jiang, R. A. Badcock, and C. W. Bumby, IEEE Transactions on Applied Superconductivity **26**, 1 (2016).
[42] J. R. Clem, Phys. Rev. B **1**, 2140 (1970).
[43] E. H. Brandt and M. Indenbom, Phys. Rev. B **48**, 12893 (1993).
[44] V. M. R. Zermeño, A. B. Abrahamsen, N. Mijatovic, B. B. Jensen, and M. P. Srensen, J. Appl. Phys. **114**, 173901 (2013).
[45] C. Plummer and J. Evetts, IEEE Trans. Magn. **23**, 1179 (1987).
[46] J. Rhyner, Physica C **212**, 292 (1993).
[47] N. M. Strickland, C. Hoffmann, and S. C. Wimbush, Rev. Sci. Instr. **85**, 113907 (2014).
[48] S. C. Wimbush and N. M. Strickland, IEEE Trans. Appl. Supercond. **27**, 8000105 (2017).
[49] F. Grilli, A. Morandi, F. D. Silvestri, and R. Brambilla, Supercond. Sci. Technol. **31**, 125003 (2018).
[50] L. Quéval, K. Liu, W. Yang, V. M. R. Zermeño, and G. Ma, Supercond. Sci. Technol. **31**, 084001 (2018).
[51] V. V. Andrianov, V. B. Zenkevich, V. V. Kurguzov, V. V. Sychev, and F. F. Ternovskiĭ, Soviet Journal of Experimental and Theoretical Physics **31**, 815 (1970).
[52] J. M. Brooks, M. D. Ainslie, Z. Jiang, A. E. Pantoja, R. A. Badcock, and C. W. Bumby, Supercond. Sci. Technol. **33**, 035007 (2020).
[53] J. Volger and P. Admiraal, Phys. Lett. **2**, 257 (1962).
[54] O. Mawardi and S. Xu, IEEE Trans. Magn. **23**, 587 (1987).
[55] R. Mataira, M. D. Ainslie, R. Badcock, and C. W. Bumby, IEEE Transactions on Applied Superconductivity **30**, 5204406 (2020).